

Crystal-Symmetry-Driven Build Orientation and its Impact on the $\{110\}\langle 100\rangle$ Goss Texture Formation and Mechanical Properties of Laser Powder Bed Fused AISI 316L

Daniel Rainer,* Jithin James Marattukalam, Dennis Karlsson, Přemysl Beran, Charles Hervochoes, Gabriella Andersson, Prabhat Pant, and Martin Sahlberg

Directional solidification in laser powder bed fusion enables precise control over the crystallographic texture. The symmetry of the processed materials crystal system facilitates the fabrication of parts with identical texture but distinct melt pool morphologies along different build orientations. This study systematically investigates and compares the $\{110\}\langle 100\rangle$ Goss texture formation of AISI 316L along three different build orientations using bi-directional scanning: i) H_{110} perpendicular to the scan direction; ii) T_{110} with the tensile direction rotated 60° relative to the build direction and 35.26° to the scan direction; iii) V_{110} parallel to the build direction. The bulk and surface characteristics are examined using neutron diffraction, microscopy, and tensile testing. T_{110} reveals a crystallographic lamellar microstructure with major $\{110\}$ and minor $\{111\}$ grains, the strongest texture along the tensile direction and the finest solidification structure. This leads to superior strength compared to H_{110} and V_{110} while preserving the ductility. Dislocation densities and induced micro-strains appear to have only a minor impact on the observed strength differences. The results show that the properties of AISI 316L with predominant $\{110\}\langle 100\rangle$ Goss texture can be optimized by altering the build orientation.

compared to conventional processing routes. Laser powder bed fusion is a widely used method for fabricating metallic parts (PBF-LB/M) due to the variety of processable materials, the high achievable density and geometrical accuracy. PBF-LB/M is an AM process where one or multiple lasers selectively melt powder material layer-by-layer according to a 3D CAD model.^[1,2] The high thermal gradients facilitate cooling rates up to 10^7 K s^{-1} ,^[3] resulting in unique microstructures and mechanical properties.^[4] Directional solidification due to anisotropic heat dissipation typically leads to anisotropic crystallographic textures, microstructures, and mechanical properties. The anisotropy can be tailored by adapting process parameters, scan strategies, and build orientation.^[5–14] In addition, both scan strategy and build direction strongly influence the development of residual stresses during processing, which further impact the mechanical performance of PBF-LB/M parts.^[15,16] Thus, tailoring part properties

for the application-specific needs requires careful optimization of the PBF-LB/M process.


Controlling the crystallographic texture during the fabrication offers an additional possibility to tailor the properties of

1. Introduction

In the past decades, additive manufacturing (AM) has gained significant attention due to its nearly unrestricted design freedom

D. Rainer, P. Pant, M. Sahlberg
Department of Chemistry - Ångström Laboratory
Uppsala University
SE-75120 Uppsala, Sweden
E-mail: daniel.rainer@kemi.uu.se

J. J. Marattukalam
Department of Materials Science and Engineering - Ångström Laboratory
Uppsala University
SE-75103 Uppsala, Sweden

 The ORCID identification number(s) for the author(s) of this article can be found under <https://doi.org/10.1002/adem.202500423>.

© 2025 The Author(s). Advanced Engineering Materials published by Wiley-VCH GmbH. This is an open access article under the terms of the Creative Commons Attribution-NonCommercial License, which permits use, distribution and reproduction in any medium, provided the original work is properly cited and is not used for commercial purposes.

DOI: 10.1002/adem.202500423

D. Karlsson
Alleima EMEA AB
Stålforskning 74, SE-81181 Sandviken, Sweden

P. Beran, C. Hervochoes
Nuclear Physics Institute CAS
Hlavni 130, CZ-250 68 Řež, Czech Republic

P. Beran
European Spallation Source ERIC
SE-221 00 Lund, Sweden

G. Andersson
Department of Physics and Astronomy
Uppsala University
SE-751 20 Uppsala, Sweden

diffraction, optical/electron microscopy and tensile testing. Differences regarding their process–structure–property relationships are highlighted.

2. Experimental Section

2.1. Powder Production and PBF-LB/M

AISI 316L powder was gas atomized as well as analyzed by EOS GmbH and the chemical composition is stated in the supplementary information. Sieving was carried out using a 63 μm mesh and the particle size distribution was measured according to ASTM B822/ISO13320 standards. The D10, D50, and D90 values were determined from the particle size distribution as 20, 40, and 60 μm , respectively.

Cuboid-shaped $60 \times 10 \times 10 \text{ mm}^3$ samples were fabricated by PBF-LB/M utilizing an EOS M100 machine equipped with a Yb-fiber laser (spot diameter 40 μm). Based on the $\{110\}$ stereographic projection of fcc materials (space group 225), three sample batches with different build orientations were fabricated, as shown in Figure 1. Generally, the tensile direction (TD) in the sample coordinate system (green arrows in Figure 1) is parallel to the longitudinal axis of the samples and the angles φ , Ω , and χ indicate rotation angles in the sample coordinate space. For the horizontal (H_{110}) and vertical build (V_{110}), the BD was parallel to Y and TD, respectively. For both H_{110} and V_{110} , SD was parallel to X. In case of the tilted (T_{110}) build, TD was rotated in an angle of 60° to BD and 35.26° to SD. To receive an identical 3D texture as for H_{110} and V_{110} , an Euler rotation ($-45^\circ, 0^\circ, -45^\circ$) was applied (see supplementary information). Furthermore, due to the necessary support structure in the case of T_{110} , all samples were fabricated with supports to minimize influences on the texture and microstructure evolution. PBF-LB/M was carried out using bi-directional laser scanning with a laser power of 107 W, 800 mm s^{-1} scan speed and 70 μm hatch spacing. The layer thickness was set to 20 μm and the chamber was flushed with Ar (999 999% purity) to reduce impurification of the samples.

2.2. Phase Composition and Crystallographic Texture

The phase composition and bulk texture analysis were carried out in a neutron powder diffractometer MEREDIT@NPI^[29] using a neutron wavelength of 1.46 Å. The powder diffraction pattern for the microstructure analysis (see below) was collected in a 2 θ range of 4° and 144° with a step size of 0.08°. During the data collection, the sample was rotated along TD to average the texture effect in the diffraction plane. Subsequently, four full pole figures of the reflections $\{111\}$, $\{200\}$, $\{220\}$, and $\{311\}$ were measured perpendicular to TD. The X direction was aligned with $\varphi = 0^\circ$. The samples were rotated along in the range 0–360° and χ in the range 0°–90°, both with a step size of 5°. Appropriate orientation distribution functions (ODF) were calculated from the pole figures and consecutively analyzed and visualized using ATEX software.^[30]

2.3. Part Density and Melt Pool Morphology

The (relative) densities of as-built sample rods were measured using the Archimedes principle after ASTM B962^[31] and the

average density of five measurements was calculated. For the evaluation of the relative density, a reference density of 7.98 g cm^{-3} was used.^[14]

For the microstructure analysis, the samples were cut in the XY-plane. Polishing was carried out using different SiC abrasive papers and diamond as well as colloidal silica suspension for fine polishing. As a final step, the sample surfaces were etched using diluted (1:1) aqua regia to reveal the melt pools. Micrographs were collected with an Olympus AX70 light optical microscope (LOM) and a ZEISS Merlin scanning electron microscope (SEM) using the Everhart Thornley secondary electron detector (SE-SEM). High-resolution SEM micrographs of the solidification cells were collected utilizing the in-lens detector of the ZEISS Merlin SEM. To determine the size of the cellular substructure, the intragranular cell spacings ICS of three different regions were calculated and averaged using the relation.

$$ICS = \left(\frac{A}{N} \right)^{1/2} \quad (1)$$

With the area of the region of interest A (in μm^2) and the number of cellular sub-grains N within the area.^[32] Electron backscatter diffraction (EBSD) was carried out using the ZEISS Merlin SEM equipped with a Nordlys Max EBSD-detector. The EBSD maps were collected using a 70° pre-tilt sample holder at 20 kV acceleration voltage with a step size of 1 μm . For H_{110} and V_{110} , the EBSD map sizes were set to $(600 \times 450) \mu\text{m}^2$ and for T_{110} , the map size was selected as $(1400 \times 1000) \mu\text{m}^2$. The resulting EBSD data was then evaluated using the MATLAB toolbox MTEX.^[33] Inverse pole figure (IPF), grain boundary (GB) and first-order kernel average misorientation (KAM) maps were generated. For the KAM maps, a careful noise reduction with a half-quadratic filter ($\alpha = 0.4$) was carried out to improve the data quality.^[34] Overall, the filtered data remained below 10 %.

2.4. Micro-Strain Analysis and Dislocation Density

The microstructure analysis of the powder diffraction pattern was performed using the FULLPROF Suite.^[35] The instrument resolution function was estimated from the full-pattern fitting of the SiO_2 standard sample at the same conditions. Anisotropic broadening of certain reflections above the instrument resolution was observed. To analyze this effect, the anisotropic strain broadening using Stephens formalism^[36,37] was adopted to determine the micro-strain contribution. The effect of the size broadening was neglected. For the evaluation, the elastic constants of austenite c_{11} (276 GPa), c_{12} (173 GPa), and c_{44} (136 GPa) were taken from the Materials Properties Open Database.^[38] The resulting reciprocal interplanar spacings d_{hkl}^* and integral breadths β^* were extracted to generate Williamson–Hall (WH) plots.^[39] The micro-strains were calculated from the slope of the linear fit. Due to anisotropic strain broadening, further refinement was carried out by taking the average contrast factors C_{hkl} of individual dislocation systems into account (modified WH approach).^[40] The average dislocation contrast factors were calculated for cubic crystal systems using ANIZC software^[41] after.

$$C_{hkl} = C_{h00}(1 - qH^2) \quad (2)$$

With the average contrast factor corresponding to h00 reflections C_{h00} , an elastic constant dependent parameter q and $H^2 = (h^2k^2 + h^2l^2 + k^2l^2)(h^2 + k^2 + l^2)^{-2}$ with the miller indices of the diffraction vector h , k and l . Different dislocation systems were mixed by linear combination and analyzed regarding χ^2 (supplementary information) to improve the data scattering. The mixed dislocation system with the minimum χ^2 was used for the micro-strain calculations. Additionally, the dislocation density ρ_d was estimated after Krivoglaz et al.^[42] (seen in Ref. [43]).

$$\beta^* = b\sqrt{\rho_d}\sqrt{C_{hkl}}\sqrt{2\ln P}\left(\frac{\sin(\theta_{hkl})}{\lambda}\right) \cdot \left(1 - \left(\frac{\ln(\ln P)}{4\ln P}\right)\right)^{-1} \quad (3)$$

With the burgers vector b , dislocation correlation factor P , diffraction angle of the individual reflections θ_{hkl} and neutron wavelength λ . The burgers vector b was calculated parallel to the primary slip direction $\langle 110 \rangle$ in fcc materials as $a/\sqrt{2}$, with the lattice parameter a (determined and averaged from the peak positions). The dislocation correlation factor P is related to the arrangement of the dislocations and can be estimated from the diffraction peak broadening. Due to the moderate resolution of the diffraction data, it was not possible to directly determine P using Fourier analysis. Instead, a P -value of 10 was estimated, which is considered reasonable for the Gaussian peak profiles used for the strain broadening analysis in this work.^[43,44]

2.5. Mechanical Properties

For tensile testing, as-printed sample rods were machined to the final dimensions according to ASTM E8M^[45] (4 mm diameter, 20 mm gauge length). Tensile testing was performed parallel to TD on three samples of each build to determine differences in the mechanical properties. The tests were carried out using a deformation rate of 0.005 mms^{-1} , corresponding to an initial strain rate of $\approx 0.00016 \text{ s}^{-1}$. The fracture elongation was estimated manually by inscribing two lines with 5 mm distance before testing and measuring the distance after failure. The strain-hardening rate SHR was calculated after converting the engineering stress/strain σ_e, ϵ_e to true stress strain values σ_t, ϵ_t .^[46]

3. Results and Discussion

3.1. Phase Composition and Crystallographic Texture

Figure 2 shows the neutron diffractograms measured perpendicular to TD (averaged along φ) with normalized intensities for H_{110} , T_{110} , and V_{110} . All samples are monophasic and reveal an austenitic fcc crystal structure, which is in agreement with previous reports of AISI 316L built by PBF-LB/M with varying build orientations^[7,10,11] and scan strategies.^[7,9,14,47] For AISI 316L fabricated by wire arc additive manufacturing (WAAM)^[48] and direct energy deposition (DED),^[49] delta ferrite formation has been reported. However, no such phase has been identified in the current or any other PBF-LB/M study. This is most likely based on the lower cooling rates in WAAM (10^2 – 10^3 K s^{-1})^[50] and DED (10^3 – 10^5 K s^{-1})^[1,51] compared to

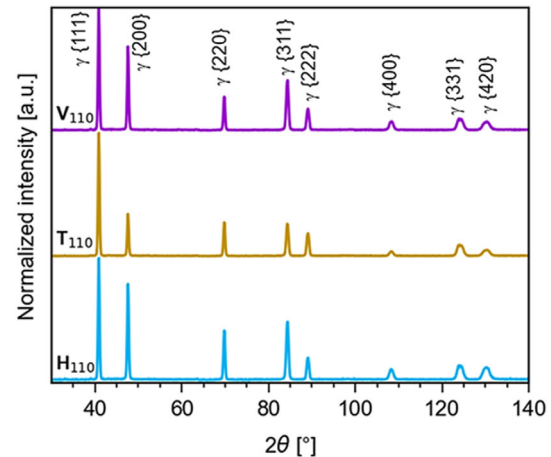


Figure 2. Neutron diffractogram with normalized intensity of H_{110} (bottom), T_{110} (center), and V_{110} (top) with indicated γ -austenite reflections. The measurements were conducted using neutrons with a wavelength of 1.46 \AA .

PBF-LB/M (10^7 K s^{-1}).^[3] The different peak intensities in the diffractograms (e.g., {200}) indicate differences in the texture dependent on the build orientation. For all samples, a $\{110\} \langle 100 \rangle$ Goss texture along TD is expected due to bidirectional scanning along SD^[14] and the crystal symmetry of cubic systems (Figure 1). Thus, texture measurements using a goniometer were carried out for in-detail analysis of the crystallographic texture along TD.

Figure 3 summarizes the results of the texture measurements with the sample coordinate system indicated at the bottom left. In Figure 3a–c, the measured neutron pole figures for the $\{100\}$, $\{110\}$, and $\{111\}$ reflections as well as the calculated one for $\{112\}$ are shown. It is evident that all three samples reveal a predominant $\{110\} \langle 100 \rangle$ Goss texture along TD. In PBF-LB/M, the observed crystallographic texture is mainly governed by the melt pool geometry, the thermal gradient G and the migration velocity of the solid–liquid interface R .^[17–20] Figure 4 provides a schematic illustration of the texture formation obtained in a previous work^[14] of AISI 316L. The nail-head shaped melt pool geometry (Figure 4a) leads to $\langle 100 \rangle$ oriented dendrites growing along BD at the centerlines while an $\approx \pm 45^\circ$ inclined $\langle 100 \rangle$ dendritic growth occurs in the surrounding regions.^[18,21,22] This results in the formation of a CLM^[19] with predominant $\{110\} \langle 100 \rangle$ Goss texture along BD and minority $\{100\}$ grains at the melt pool centerlines (Figure 4b). The CLM formation also explains the observed grain orientation spread in the IPFs (Figure 3d,f) for H_{110} and V_{110} as well as the increased intensity of the $\{200\}$ peak in the diffraction pattern in Figure 2. Comparing the IPF of V_{110} (Figure 3f) with other CLMs,^[19,52] the texture appears less distinct in this work. In PBF-LB/M, the used process parameters are decisive for the obtained texture in the CLM.^[12,52] However, in this work the parameters were optimized to achieve the highest possible density along all three build orientations (see Table 1). For T_{110} , the grain orientation distribution is spread toward $\{111\}$ rather than $\{100\}$. A similar result was reported by Dixit et al.^[10] for tensile rods where TD was rotated 45° relative to SD. They suggested that the texture variations might be caused by the change in number of hatch stripes, an altered direction of the steepest thermal

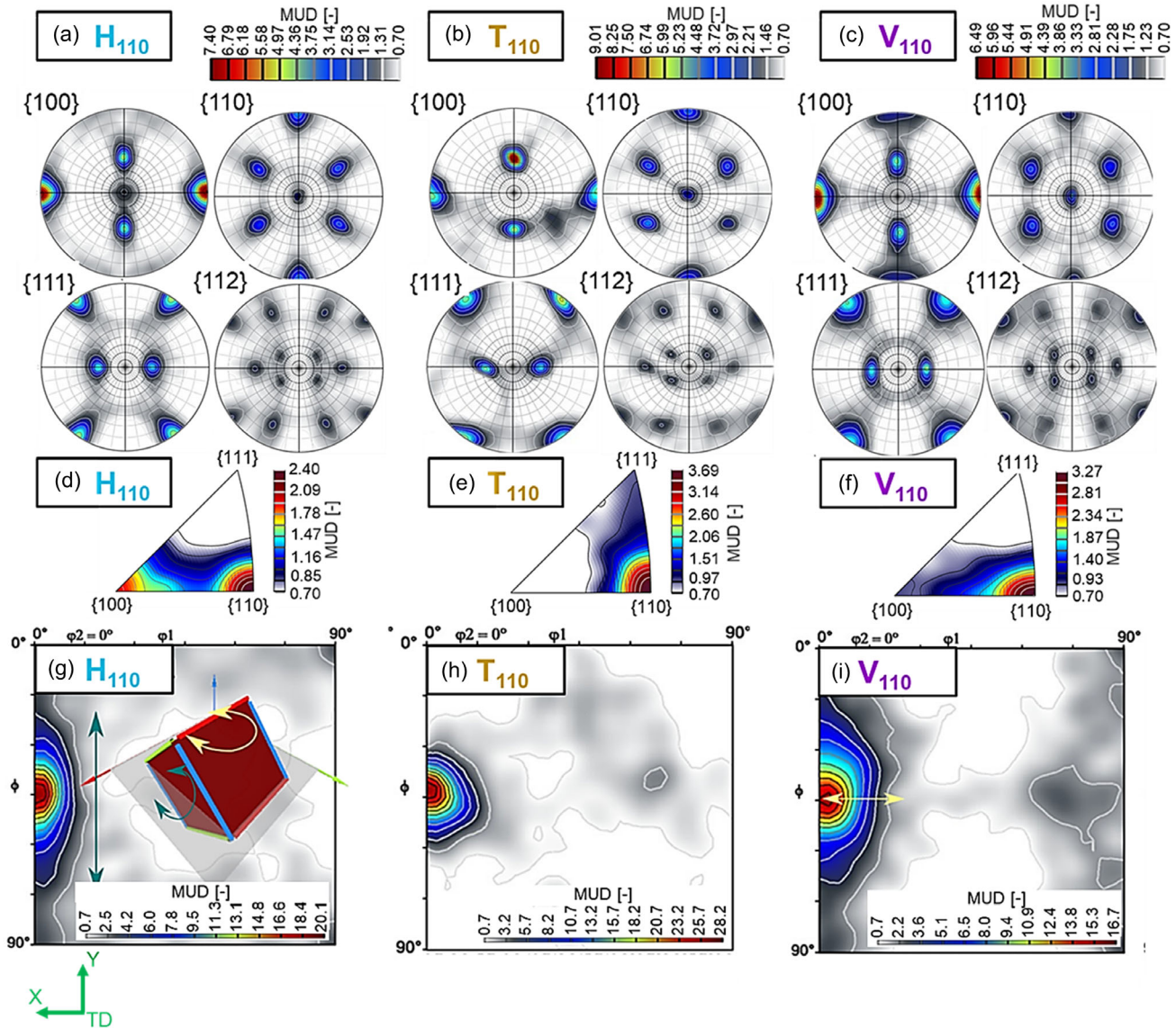


Figure 3. a–c) $\{100\}$, $\{110\}$, $\{111\}$, $\{112\}$ pole figures. d–f) IPFs and g–i) corresponding ODFs of H_{110} (a,d,g), T_{110} (b,e,h), and V_{110} (c,f,i). The green sample coordinate system is valid for all pole figures and ODFs.

gradient G and the varying heat input per layer. The ODFs in Figure 3g–i illustrate the orientation of individual crystallites in H_{110} , T_{110} , and V_{110} . Furthermore, the texture strength of the individual samples can be evaluated by the multiple of uniform density (MUD). It is evident that the T_{110} sample exhibits the least orientation spread and thus the strongest $\{110\}\langle 100 \rangle$ Goss texture with a maximum MUD of 28.2 in Figure 3h. In contrast, the V_{110} sample displays the largest orientation spread and thus the weakest texture with a maximum MUD of 16.7 in Figure 3i. To enable a more standardized comparison of texture strength, the texture indices J were calculated as 2.9 for H_{110} , 4.1 for T_{110} , and 2.5 for V_{110} (see supplementary information for calculation details). Nadammal et al.^[5] reported that a larger hatch length results in weaker textures for IN718. In this work, the hatch lengths of H_{110} and V_{110} are identical and alternate for

T_{110} (Figure 3b), not explaining the observed trend. One possible reason for texture variations might be the direction of the gas flow, as reported by Amano et al.^[53] for AISI 316L. Additionally, it has been suggested that the G/R ratio is crucial for the texture formation in Al samples, resulting in $\{111\}$ for higher, $\{110\}$ for intermediate and $\{100\}$ texture for lower G/R .^[17] Furthermore, the ratio G/R as well as the product $G \times R$ also play an important role in the morphology and size of the microstructure. Therefore, this is further investigated in the next section.

3.2. Part Density and Melt Pool Morphology

The quality of a part is frequently assessed by the achieved density of the final part.^[54] Table 1 shows the absolute as well

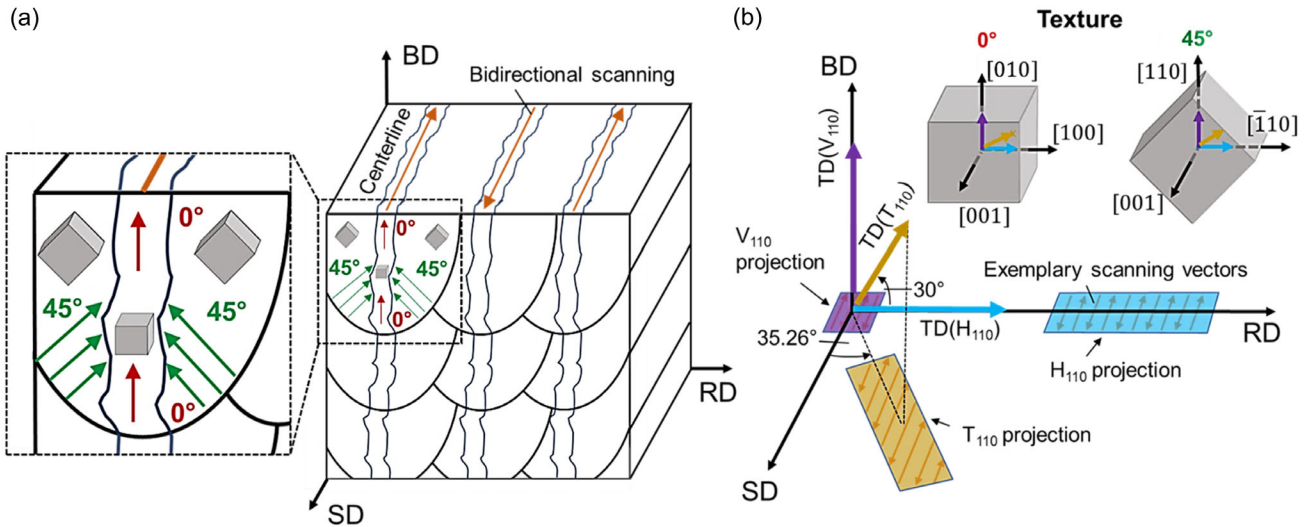


Figure 4. a) Schematic illustration of the texture formation for bidirectional scanning from a previous work^[14] with identical printing parameters and b) the connection to the build orientation for H_{110} , T_{110} , and V_{110} .

Table 1. Densities measured by Archimedes principle and the relative densities of H_{110} , T_{110} , and V_{110} . For the relative densities, a reference density of 7.98 g cm^{-3} was used.^[14]

	H_{110}	T_{110}	V_{110}
$\rho \text{ [g cm}^{-3}\text{]}$	7.974 ± 0.005	7.972 ± 0.004	7.972 ± 0.005
rel. $\rho \text{ [%]}$	99.92 ± 0.06	99.90 ± 0.05	99.90 ± 0.06

as relative density of H_{110} , T_{110} , and V_{110} . In this work, all samples are fully dense ($\rho \geq 99.9\%$) which is in agreement with a previous report using the identical experimental setup.^[14] Previous studies have shown that the build orientation might influence the part density^[28,55–57] and further, the ductility of AISI 316L.^[57] In this work, the ductility of all samples is comparable (see mechanical properties section) and thus this effect could not be observed.

Figure 5 depicts LOM (a–c) and SE-SEM (d–f) micrographs of exemplary H_{110} (a,d), T_{110} (b,e) and V_{110} (c,f) samples in the XY-plane. The microstructure of PBF-LB/M AISI 316L is highly hierarchical, exhibiting features ranging from a few hundred micrometers (melt pools) to submicron cellular and columnar solidification structures.^[4,10,13,14,47] The varying build orientations result in distinct melt pool morphologies for H_{110} , T_{110} , and V_{110} . In H_{110} (Figure 5a), the melt pool boundaries form long bands parallel to X (SD) due to the laser scanning. The wavy shape of these bands can be explained by melt pool flows during laser scanning, such as the Marangoni convection flow.^[1,14,17,22] Additionally, columnar grains spanning over several melt pools with a size of a few hundred μm are apparent, indicating epitaxial grain growth which is frequently observed in PBF-LB/M (Figure 5a,d).^[10,13,14,18,22,23,58] In Figure 5b,c,e,f, the micrographs of T_{110} and V_{110} show the formation of a CLM^[19] with minor grains at the melt pool centerlines (white dashed line). A more detailed micrograph of the CLM and the melt pool morphology of T_{110} is shown in **Figure 6**. For V_{110} (Figure 5c), the

melt pool morphology with minor grains at the centerlines is similar to the ‘standard’ CLM.^[19] The results demonstrate the potential to print CLMs with various build orientations which is a key outcome of this work.

Figure 7a–c reveals SEM micrographs of the solidification structure of H_{110} , T_{110} , and V_{110} . The cellular and columnar solidification structure is a unique feature of PBF-LB/M and has been frequently discussed in literature for AISI 316L.^[4,9–11,13,14,18,59,60] In various publications, the size of the cellular solidification structure has been pointed out as possible determining factor of the mechanical properties of PBF-LB/M parts.^[4,10,59,60] Thus, the average ICS of three different regions (one example is marked in Figure 7b) is shown in Figure 7d. The average ICS show a clear trend with the smallest size of the cellular solidification structure in T_{110} and the largest one in V_{110} . Compared to G/R which defines the morphology, the product $G \times R$ correlates inversely with the size of the solidification structure.^[17] In this work, the varying ICS (Figure 7d) and the matching trend with the texture strength (finer solidification structure and stronger texture) reinforces the discussion about G and R variations depending on the build orientation. Thus, by controlling the build orientation (H_{110} , T_{110} , V_{110}) and consequently G and R , the size of the solidification structure can be finetuned which can be used to improve the performance of PBF-LB/M parts.

The EBSD analysis in **Figure 8** provides deeper insights into the crystallographic orientation of individual grains and locally induced micro-strains by dislocations. Figure 8a,d,g show IPF maps of H_{110} , T_{110} and V_{110} , respectively. The IPF color legend represents the crystallographic orientation along TD. The large columnar grains shown in Figure 5 reveal predominantly $\{110\}$ orientation. The minority $\{100\}$ grains in H_{110}/V_{110} and $\{111\}$ grains in T_{110} match with the results of the neutron diffraction experiments (Figure 3d–f) and the EBSD pole figures (supplementary information). Figure 8b,e,h depict GB maps with low-angle grain boundaries (2° – 15° , LAGBs) as well as high-angle

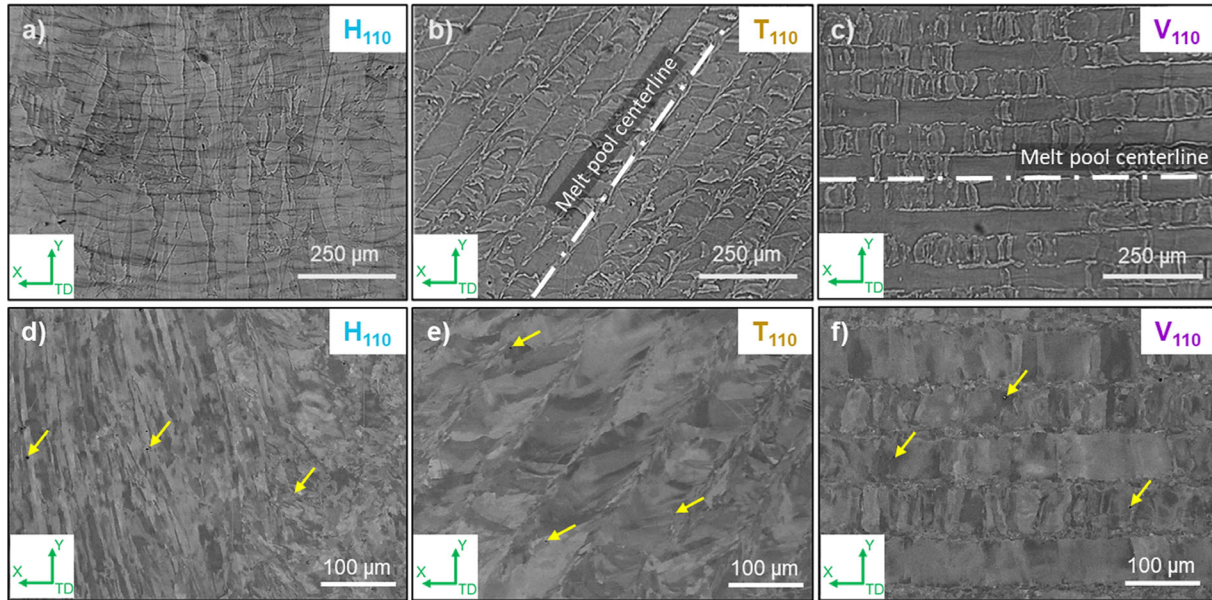


Figure 5. a–c) LOM and d–f) SE-SEM images of etched (a,d) H₁₁₀, (b,e) T₁₁₀ and (c,f) V₁₁₀ samples. The white dashed line indicates an exemplary melt pool centerline and the yellow arrows indicate pores.

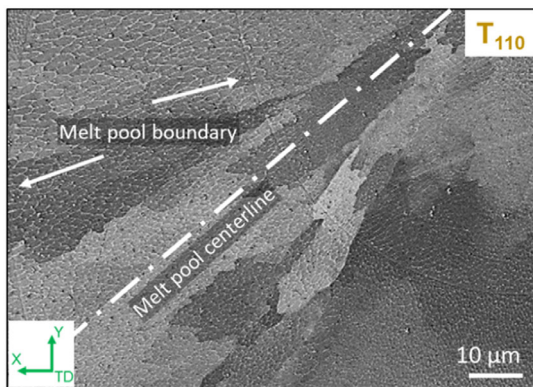


Figure 6. Detailed micrograph of the CLM and solidification structure in T₁₁₀.

grain boundaries ($>15^\circ$, HAGBs) with the total fractions stated below. High fractions of LAGBs are obtained for all samples ($\geq 60\%$) which can be explained by the directional solidification during PBF-LB/M and consequently small orientation differences of adjacent grains.^[11,13,60] This is also the reason that LAGBs accumulate between minor grains at the melt pool centerlines in T₁₁₀ and V₁₁₀.^[13,52] The KAM maps in Figure 8c,f,i reveal the spatial strain distribution in the XY-plane, indicating a correlation with the spatial distribution of LAGBs. This is frequently observed in PBF-LB/M^[4,11] and based on the accumulation of dislocations at LAGBs.^[11] However, there is no correlation with the texture strength apparent which might be based on the bimodal grain size distribution in case of T₁₁₀ and V₁₁₀. Furthermore, due to their small size, grains at the centerlines will contribute stronger to the GB fractions than the surrounding larger columnar grains.

3.3. Micro-Strain Analysis and Dislocation Density

The anisotropic peak broadening in the diffractograms (Figure 2) indicates locally induced micro-strains by dislocations^[44] which are also apparent in the KAM maps (Figure 8). In Figure 9, the maximum micro-strains are quantified by a modified WH approach,^[40] considering the dependence of β^* on $d^* \times C_{hkl}^{1/2}$ with the average dislocation contrast factors C_{hkl} . WH plots are a standard method for analyzing peak broadening effects in diffractograms caused by the size of coherent scattering domains and micro-strains.^[7,10,39,43,44,61,62] The composition of the predominant dislocation system of 70% screw $\langle 110 \rangle$ and 30% edge $\langle 110 \rangle \{111\}$ dislocations was determined by minimizing the linear fit parameter χ^2 (supplementary information). The resulting predominant dislocation system matches with the $\langle 110 \rangle$ primary slip direction of fcc materials.^[63] The calculated maximum micro-strains in all modified WH plots reveal the order T₁₁₀ < H₁₁₀ < V₁₁₀ with only a minor difference between H₁₁₀ and V₁₁₀. Considering the determined Young's moduli (E) of each sample in Table 3, the maximum micro-strains in Figure 9 correspond to micro-stresses in the range of 400 MPa calculated by Hooke's law (supplementary information). The high micro-stresses are related to the high dislocation densities (Table 2) and can be explained by the nature of the PBF-LB/M process. The calculated dislocation densities for the predominant dislocation system are shown in Table 2 along with other key microstructural parameters, including part density ρ , texture index J , ICS, GB fractions and average Taylor factors M_{avg} . A detailed explanation of the Taylor model can be found in the supplementary information. Two main contributions for the high dislocation densities were pointed out in literature:^[10] I) Segregation at the solidification cell walls lead to coherency strains facilitating local dislocation formation and II) residual stresses due steep thermal gradients and following accumulation

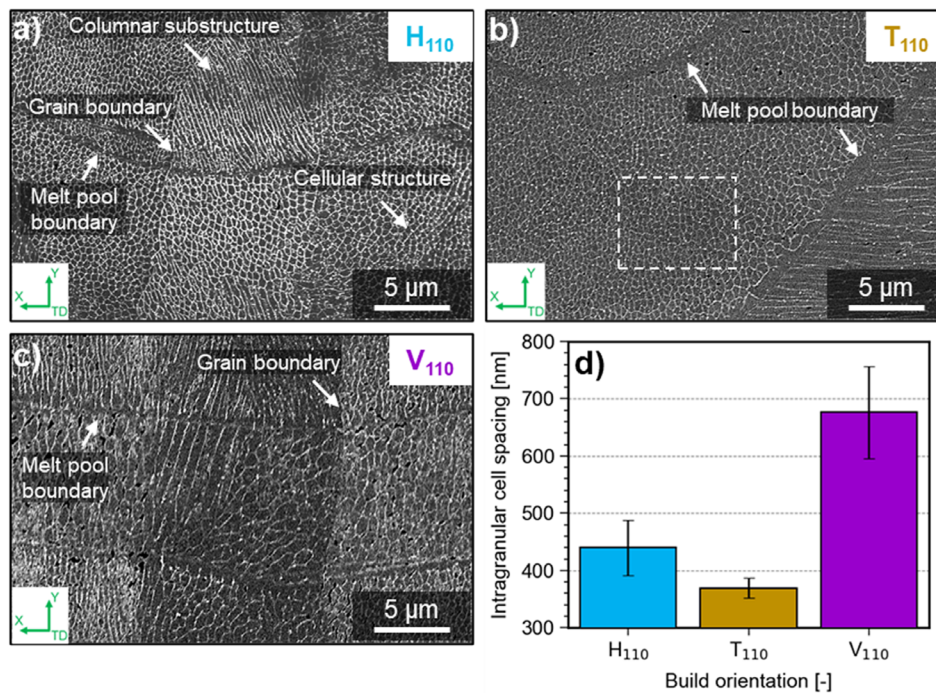


Figure 7. High-resolution SEM images of the solidification structure for a) H₁₁₀, b) T₁₁₀ as well as c) V₁₁₀ and d) the calculated intragranular cell spacings (ICS) along TD. An exemplary area for the ICS calculation is illustrated by the white dashed rectangle in (b).

by dislocations. The segregation and the residual stresses are closely related to G and R . This implies that the differences in micro-strains as well as dislocation densities are governed by the earlier discussed G and R variations. Regarding the calculation of the dislocation density, a high error margin between 20%–50% was estimated.^[44] This is mainly caused by the difficulty in determining the P -factor in Equation (3) and the experimental limitations of the neutron diffraction setup. However, the trend is independent of constant values and the order of magnitude of the dislocation densities is identical to former results of AISI 316L.^[7,48,60]

3.4. Mechanical Properties

The observed microstructural differences between the samples are expected to influence the mechanical behavior. Therefore, tensile test results of sample batches (three each) are shown in **Figure 10**, with the averaged quantities listed in **Table 3**. Figure 10a shows the engineering stress–strain curves. For comparison, results from previously studied fiber and {100}-textured samples are also included and briefly discussed here; further details can be found in the referenced study.^[14]

The average Young's modulus E of T₁₁₀ is larger than that of H₁₁₀, while the high standard deviation for V₁₁₀ does not indicate a clear trend. Furthermore, all three values are significantly higher than those of the {100}-textured samples. Generally, E is closely related to the stiffness of interatomic bonds along specific crystallographic directions and is thus highly anisotropic. In cubic materials, E is higher along directions with higher atomic packing density ($E_{100} < E_{110} < E_{111}$).^[10,14] This trend aligns with the IPFs in Figure 3d–f indicating that T₁₁₀ exhibits the highest

fraction of {111} grains and H₁₁₀ reveals the highest fraction of {100} grains.

Compared to H₁₁₀ and V₁₁₀, T₁₁₀ shows superior yield strength YS and ultimate tensile strength UTS while preserving the ductility ($\approx 45\%$ uniform elongation at fracture UE). This trend is also reflected in the strain-hardening rate SHR, shown in Figure 10b, which was calculated from true stress–strain curves. Estimates of the onsets and offsets of the different stages (Stage I, II and III) are indicated by dashed lines. In PBF-LB/M AISI 316L, the main strengthening mechanisms have been extensively studied and are commonly identified as texture effects,^[10,14,23,64] GB strengthening,^[4,11,60,65] dislocation strengthening,^[4,10,11,64,65] and particle strengthening.^[4]

In the present study, differences in crystallographic texture were observed between the three build orientations, which may contribute to the strength variation. T₁₁₀ exhibits a stronger overall texture and {111} grains along the tensile direction, which are not observed in the other samples. Previous studies have shown that the $\langle 111 \rangle$ orientation is generally associated with increased resistance to slip initiation due to lower Schmid factors.^[23] According to their calculation, $\langle 111 \rangle$ orientations exhibit a maximum Schmid factor of 0.272 compared to $\langle 100 \rangle$ and $\langle 110 \rangle$ orientations (both 0.408). The higher slip resistance in {111} grains might contribute to the higher strength of T₁₁₀. However, no clear variation in ductility was observed among the samples, contrary to expectations (e.g., {100}-textured sample in Figure 10a).

GB strengthening is primarily attributed to HAGBs, which act as effective barriers to dislocation motion due to the large misorientation between adjacent grains. In contrast, LAGBs provide only limited resistance to dislocation slip, owing to their relatively

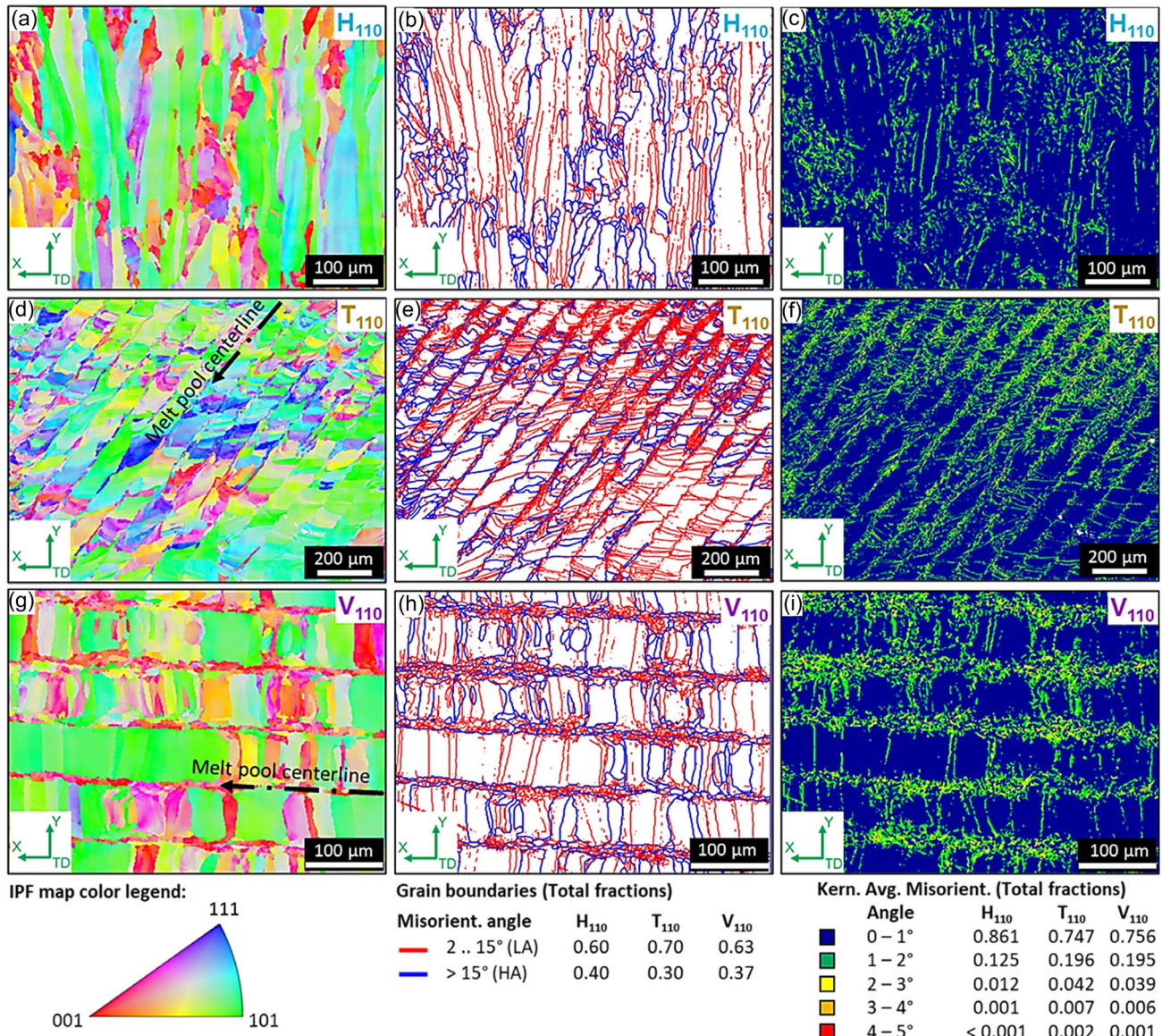


Figure 8. a,d,g) IPF, b,e,h) GB, and c,f,i) KAM maps of H₁₁₀ (a–c), T₁₁₀ (d–f) and V₁₁₀ (g–i). The IPF color legends represents the crystallographic orientations along TD. The black arrows in (d) and (g) indicate the melt pool centerline.

low misorientation.^[11] In this work, T₁₁₀ shows the lowest fraction of HAGBs (Figure 8), which does not align with the highest strength observed for T₁₁₀. Furthermore, the length of the mean free dislocation path^[11] on this length scale does not directly correlate with the observed strength difference of H₁₁₀ and T₁₁₀ (Figure 11). Wang et al.^[4] stated that strengthening of PBF-LB/M AISI 316L has to be evaluated on multiple length scales, including the solidification structure. In several works, the cellular solidification structure was reported as one of the predominant strengthening factors in PBF-LB/M of AISI 316L.^[4,14,65–67] In this study, the trend of the decreasing cellular solidification cell size correlates with an increasing strength similar to a Hall-Petch relation^[4,14] (see supplementary file). It has been shown that the solidification structure of AISI 316L mainly consists of LAGBs (<2° misorientation angle) and block boundaries

exhibiting larger misorientation angles up to 4°.^[65] These relatively low misorientation angles most likely offer limited resistance to dislocation motion, suggesting only a modest contribution to overall strengthening. However, the dislocation network along the solidification cell boundaries and the associated dislocation entanglement hinders dislocation motion, contributing to strengthening.^[66,67] At the same time, the LAGBs still allow a continuous flow of dislocations, enabling strength enhancement without sacrificing ductility. This characteristic was stated as one of the key advantages of PBF-LB/M over conventionally manufactured AISI 316L, which typically exhibit a strength–ductility tradeoff.^[66]

Dislocation strengthening is based on interactions between dislocations acting as mutual obstacles.^[63] The rapid cooling rates during PBF-LB/M processing yield high dislocation

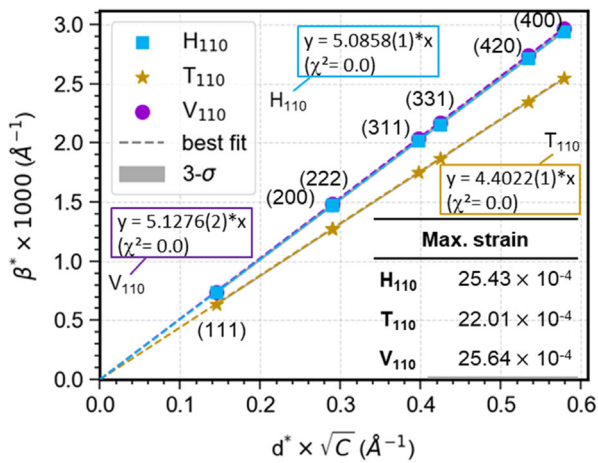


Figure 9. Modified WH plot for 70% screw<110> and 30% edge<110>{111} dislocations in H₁₁₀, T₁₁₀, and V₁₁₀. The maximum microstrains were determined from the slope of the linear fit. Due to mixing of the dislocation systems and optimization of χ^2 , 3- σ coincides with the linear fit.

Table 2. Comparison table of the quantitative microstructure analysis including the texture index J , part densities ρ , intragranular cell spacings ICS , high-angle and low-angle grain boundary fractions HAGBs/LAGBs, dislocation densities of the predominant dislocation system (70% screw<110> and 30% edge<110>{111}) ρ_d and the average Taylor factors M_{avg} .

Metrics	H ₁₁₀	T ₁₁₀	V ₁₁₀
J [-]	2.9	4.1	2.5
ρ [g cm ⁻³]	7.974 ± 0.005	7.972 ± 0.004	7.972 ± 0.005
ICS [nm]	440 ± 60	370 ± 20	680 ± 100
HAGB fraction [-]	0.40	0.30	0.37
LAGBs fraction [-]	0.60	0.70	0.63
ρ_d [m ⁻²]	3 × 10 ¹⁴	2 × 10 ¹⁴	3 × 10 ¹⁴
M_{avg} [-]	2.4	2.5	2.3

densities resulting in higher strengths than those of conventionally fabricated parts.^[4,10,11,64,65] In this study, no direct correlation can be found between the dislocation densities calculated from neutron diffraction data (Table 2) and the measured strength values. In textured polycrystalline materials, dislocation strengthening is also linked with a texture dependent Taylor factor M , as described by the Taylor strengthening model (see supplementary information).^[10,14] The average Taylor factors for H₁₁₀, T₁₁₀, and V₁₁₀ are 2.4, 2.52, and 2.3, corresponding to estimated strengthening contributions of 199 MPa, 171 MPa, and 191 MPa, respectively. Notably, these values do not align with the observed strength trend, particularly the highest strength in T₁₁₀, suggesting that other mechanisms may play a more significant role.

Particle strengthening in AISI 316L is based on precipitation of transition-metal-rich silicate nanoparticles which act as dislocation pinning sites and promote twinning. The latter was identified as only a minor contribution to the mechanical strength of AISI 316L (5–10 MPa).^[4] Due to the different thermal histories of different build orientations, it is expected that there is a difference in particle strengthening of H₁₁₀, T₁₁₀, and V₁₁₀. However, the contribution is most likely small and thus high-resolution analysis was considered to be out of the scope of this study.

The SHR in Figure 10b provides insights into the strain-hardening behavior of H₁₁₀, T₁₁₀ and V₁₁₀. In Stage (I), all three

Table 3. Average Young's modulus E , yield strength YS , ultimate tensile strength UTS , and elongation at fracture UE of the different sample batches. The data of the {100} and fiber textured batches was taken from Ref. [14].

Sample batch	E [GPa]	YS [MPa]	UTS [MPa]	UE [%]
H ₁₁₀	164 ± 10	540 ± 3	596 ± 2	45 ± 4
T ₁₁₀	198 ± 9	566 ± 9	650 ± 5	45 ± 2
V ₁₁₀	183 ± 22	500 ± 10	573 ± 6	46 ± 3
{100} texture ^[14]	129 ± 3	554 ± 5	649 ± 3	26 ± 1
Fiber texture ^[14]	193 ± 16	603 ± 2	690 ± 2	32 ± 2

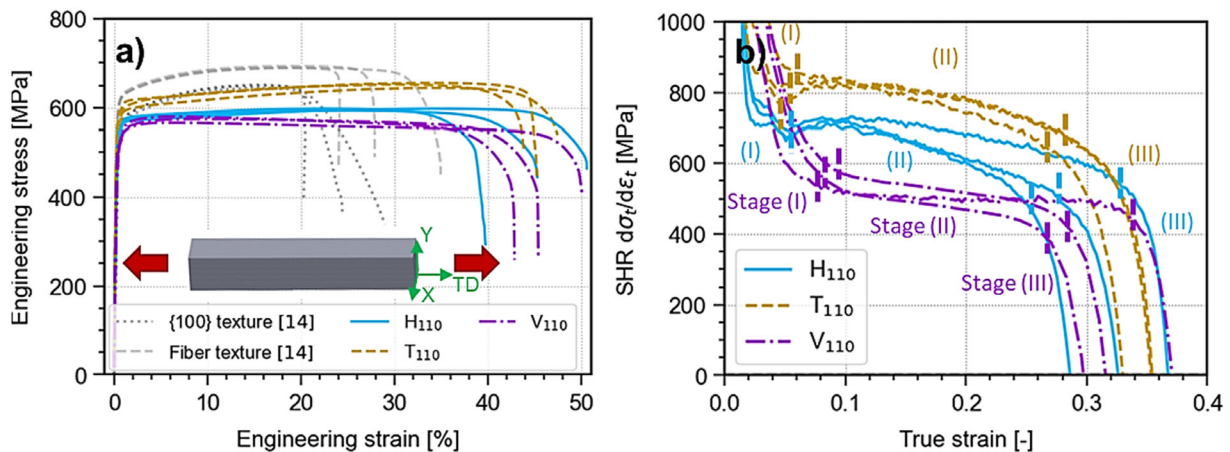


Figure 10. a) Stress–strain curves of the H₁₁₀, T₁₁₀, V₁₁₀ sample batches and the {100} as well as fiber texture of a preliminary study^[14]. Furthermore, b) strain-hardening rates of H₁₁₀, T₁₁₀, and V₁₁₀. The red arrow in (a) indicates the direction of tensile testing.

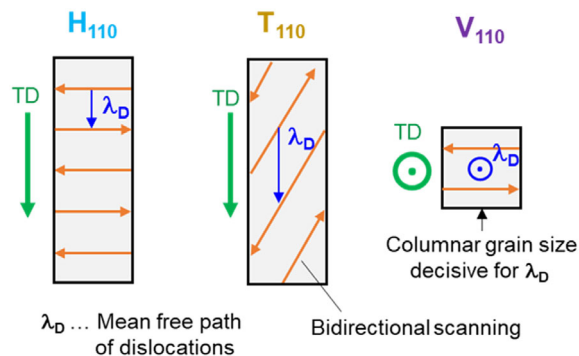


Figure 11. Schematic illustration of the mean free path of dislocations solely considering the grain boundaries, which are governed by the melt pool morphology.

batches exhibit a sharply decreasing SHR, typically attributed to dislocation rearrangement at the onset of plastic deformation.^[23,68–72] During stage (II), the SHR increases for H_{110} and T_{110} , while V_{110} shows a nearly monotonic decrease. This stage is primarily governed by deformation twinning, where the formation of twin boundaries impedes dislocation motion and thus enhances strain hardening.^[23,68,70,72] Twinning is highly dependent on the crystallographic orientation of individual grains with $\{110\}$ and $\{111\}$ orientations more favorable for twinning than $\{100\}$, due to the lower critical resolved shear stress required.^[23] Thus, the varying texture strengths ($V_{110} < H_{110} < T_{110}$) and the additional $\{111\}$ grains in T_{110} (Figure 3g–i) are most likely the primary contribution to the strain-hardening differences in this stage. The subsequent decline in SHR in both H_{110} and T_{110} during the latter part of stage II suggests saturation of twinning activity, with dislocation slip becoming the dominant deformation mechanism.^[23,68,70,72] Notably, although twinning is generally associated with enhanced ductility through the twinning-induced plasticity (TWIP) effect,^[23] no such improvement in ductility was observed for either H_{110} or T_{110} . This may be attributed to limited twin volume fractions or insufficient twin activity to significantly contribute to strain accommodation. Stage (III) is characterized by a steep decrease in SHR for all samples, which is associated with the onset of necking after surpassing the UTS.^[23]

4. Conclusions

This study introduces a crystal-symmetry-based approach to select build orientations that result in distinct thermal histories while maintaining an identical predominant $\{110\}<100>$ Goss texture in AISI 316L. This strategy enables a more targeted optimization of mechanical performance in textured PBF-LB/M components and can be extended to other alloy systems. Three different sample batches were fabricated: i) H_{110} built perpendicular to SD; ii) T_{110} with TD rotated 60° relative to BD and 35.26° relative to SD; iii) V_{110} built along BD. Bulk neutron diffraction experiments were combined with microscopy and tensile testing to gather a complete picture of the process–structure–property relationships. Compared to H_{110} and V_{110} , T_{110} reveals the formation of a CLM with predominant

$\{110\}<100>$ Goss texture and $\{111\}$ minority grains at the melt pool centerlines. Additionally, T_{110} reveals the finest solidification structure of all three samples. The texture variations and solidification structure size yields increased YS, UTS and SHR of T_{110} while maintaining the high ductility (UE at fracture of 45%). The results indicate that the size of the solidification structure is the primary factor contributing to the increased mechanical strength of T_{110} .

Supporting Information

Supporting Information is available from the Wiley Online Library or from the author.

Acknowledgements

This research is funded by the European Union under GA 101081419. Views and opinions expressed are however those of the author(s) only and do not necessarily reflect those of the European Union or REA. Neither the European Union nor the granting authority can be held responsible for them. The authors would also like to acknowledge VR (#2022-03069_VR) for funding parts of the project. The neutron measurements were carried out at the CANAM infrastructure of the NPI CAS Rez. The employment of the CICRR infrastructure supported by MEYS project LM2023041 is acknowledged. Furthermore, the authors acknowledge Myfab Uppsala for providing facilities and experimental support. Myfab is funded by the Swedish Research Council (2019-00207) as a national research infrastructure. The authors also want to acknowledge Mikael Ottosson for his contributions in the project and for the insightful scientific discussions.

Conflict of Interest

The authors declare no conflict of interest.

Author Contributions

Daniel Rainer: data curation (lead); formal analysis (lead); investigation (equal); writing—original draft (lead); writing—review & editing (equal). **Jithin James Marattukalam:** investigation (equal). **Dennis Karlsson:** investigation (supporting). **Přemysl Beran:** formal analysis (supporting); writing—review & editing (equal). **Charles Hervoches:** investigation (supporting). **Gabriella Andersson:** supervision (supporting); writing—review & editing (equal). **Prabhat Pant:** formal analysis (supporting); writing—review & editing (equal). **Martin Sahlberg:** conceptualization (lead); funding acquisition (lead); supervision (lead); writing—review & editing (equal).

Data Availability Statement

The data that support the findings of this study are available from the corresponding author upon reasonable request.

Keywords

additive manufacturing, bi-directional scanning, crystallographic orientation, selective laser melting, solidification structure, texture control

Received: February 12, 2025
Revised: June 17, 2025
Published online: August 17, 2025

- [1] I. Gibson, D. Rosen, B. Stucker, M. Khorasani, *Additive Manufacturing Technologies*, Springer Nature Switzerland AG, Cham, Switzerland **2020**.
- [2] A. Gebhardt, *Understanding Additive Manufacturing*, Carl Hanser Verlag, Munich, Germany **2011**.
- [3] H. Chen, D. Gu, D. Dai, C. Ma, M. Xia, *Mater. Sci. Eng. A* **2017**, *682*, 279.
- [4] Y. M. Wang, T. Voisin, J. T. McKeown, J. Ye, N. P. Calta, Z. Li, Z. Zeng, Y. Zhang, T. T. Roehling, R. T. Ott, M. K. Santala, P. J. Depond, M. J. Matthews, A. V. Hamza, T. Zhu, *Nat. Mater.* **2018**, *17*, 63.
- [5] N. Nadammal, S. Cabeza, T. Mishurova, T. Thiede, A. Kromm, C. Seyfert, L. Farahbod, C. Haberland, J. A. Schneider, P. D. Portella, G. Bruno, *Mater. Des.* **2017**, *134*, 139.
- [6] N. Nadammal, T. Mishurova, T. Fritsch, I. Serrano-Munoz, A. Kromm, C. Haberland, P. D. Portella, G. Bruno, *Addit. Manuf.* **2021**, *38*, 101792.
- [7] D. Kumar, G. Shankar, K. G. Prashanth, S. Suwas, *J. Alloys Compd.* **2024**, *976*, 173040.
- [8] L. Thijs, M. L. Montero Sistiaga, R. Wauthle, Q. Xie, J.-P. Kruth, J. Van Humbeeck, *Acta Mater.* **2013**, *61*, 4657.
- [9] D. Wang, C. Song, Y. Yang, Y. Bai, *Mater. Des.* **2016**, *100*, 291.
- [10] S. Dixit, S. Liu, H. A. Murdoch, P. M. Smith, *Mater. Sci. Eng. A* **2023**, *880*, 145308.
- [11] R. S. Thanumoorthy, J. K. Chaurasia, V. Anil Kumar, P. I. Pradeep, A. S. S. Balan, B. Rajasekaran, A. Sahu, S. Bontha, *J. Mater. Eng. Perform.* **2024**, *33*, 7930.
- [12] W. Shao, B. He, C. Qiu, Z. Li, *Opt. Laser Technol.* **2022**, *156*, 108609.
- [13] C. Zhao, Y. Bai, Y. Zhang, X. Wang, J. M. Xue, H. Wang, *Mater. Des.* **2021**, *209*, 109999.
- [14] J. J. Marattukalam, D. Karlsson, V. Pacheco, P. Beran, U. Wiklund, U. Jansson, B. Hjörvarsson, M. Sahlberg, *Mater. Des.* **2020**, *193*, 108852.
- [15] J. Robinson, I. Ashton, P. Fox, E. Jones, C. Sutcliffe, *Addit. Manuf.* **2018**, *23*, 13.
- [16] M. N. Doğu, S. Ozer, M. A. Yalçın, K. Davut, M. A. Obeidi, C. Simsir, H. Gu, C. Teng, D. Brabazon, *J. Mater. Res. Technol.* **2024**, *33*, 5457.
- [17] P. V. Cobbinah, S. Matsunaga, Y. Yamabe-Mitarai, *Adv. Eng. Mater.* **2023**, *25*, 2300819.
- [18] K. A. Sofinowski, S. Raman, X. Wang, B. Gaskey, M. Seita, *Addit. Manuf.* **2021**, *38*, 101809.
- [19] S. H. Sun, T. Ishimoto, K. Hagihara, Y. Tsutsumi, T. Hanawa, T. Nakano, *Scr. Mater.* **2019**, *159*, 89.
- [20] O. Gokcekaya, T. Ishimoto, S. Hibino, J. Yasutomi, T. Narushima, T. Nakano, *Acta Mater.* **2021**, *212*, 116876.
- [21] T. Ishimoto, K. Hagihara, K. Hisamoto, T. Nakano, *Addit. Manuf.* **2021**, *43*, 102004.
- [22] J. Wang, R. Zhu, Y. Liu, L. Zhang, *Adv. Powder Mater.* **2023**, *2*, 100137.
- [23] X. Wang, J. A. Muñoz-Lerma, M. Attarian Shandiz, O. Sanchez-Mata, M. Brochu, *Mater. Sci. Eng. A* **2019**, *766*, 138395.
- [24] S. Tekumalla, J. E. Chew, S. W. Tan, M. Krishnan, M. Seita, *Addit. Manuf.* **2022**, *59*, 103111.
- [25] P. S. Korinko, S. H. Malene, *J. Fail. Anal. Prev.* **2001**, *1*, 61.
- [26] F. Abe, K. Osakada, M. Shiomi, K. Uematsu, M. Matsumoto, *J. Mater. Process. Technol.* **2001**, *111*, 210.
- [27] D. Herzog, V. Seyda, E. Wycisk, C. Emmelmann, *Acta Mater.* **2016**, *117*, 371.
- [28] S. Ren, Y. Chen, T. Liu, X. Qu, *Metall. Mater. Trans. A* **2019**, *50*, 4388.
- [29] P. Beran, S. A. Ivanov, P. Nordblad, S. Middey, A. Nag, D. D. Sarma, S. Ray, R. Mathieu, *Solid State Sci.* **2015**, *50*, 58.
- [30] B. Beausir, J. J. Fundenberger, *ATEX-software*, Vol. 201, Université de Lorraine-Metz **2017**, p. 7, www.atex-software.eu.
- [31] ASTM International, *B962-17 Standard* **2017**, Vol. i, p. 1.
- [32] D. G. McCartney, J. D. Hunt, *Acta Metall.* **1981**, *29*, 1851.
- [33] F. Bachmann, R. Hielscher, H. Schaeben, *Solid State Phenom.* **2010**, *160*, 63.
- [34] R. Hielscher, C. B. Silbermann, E. Schmidla, J. Ihlemann, *J. Appl. Crystallogr.* **2019**, *52*, 984.
- [35] J. Rodríguez-Carvajal, *Physica B* **1993**, *192*, 55.
- [36] P. W. Stephens, *J. Appl. Crystallogr.* **1999**, *32*, 281.
- [37] J. Rodríguez-Carvajal, M. T. Fernandez-Diaz, J. L. Martinez, *J. Phys.: Condens. Matter.* **1991**, *3*, 3215.
- [38] G. Pepponi, S. Gražulis, D. Chateigner, *Nucl. Instrum. Methods Phys. Res., Sect. B* **2012**, *284*, 10.
- [39] G. K. Williamson, W. H. Hall, *Acta Metall.* **1953**, *1*, 22.
- [40] T. Ungár, *Phys. Status Solidi A* **1999**, *171.2*, 425.
- [41] A. Borbély, J. Dragomir-Cernatescu, G. Ribárik, T. Ungár, *J. Appl. Crystallogr.* **2003**, *36*, 160.
- [42] M. A. Krivoglaz, O. V. Martynenko, K. Ryaboshapka, *Fiz. Met. Met* **1983**, *55*, 5.
- [43] R. Kužel, *Zeitschrift für Kristallographie* **2007**, *222*, 136.
- [44] P. Strunz, L. Kunčická, P. Beran, R. Kocich, C. Hervoches, *Materials* **2020**, *13*, 208.
- [45] ASTM International, *ASTM E8/E8M-10 Standard* **2010**, Vol. i, p. 1.
- [46] I. Faridmehr, M. Hanim Osman, A. Bin Adnan, A. Farokhi Nejad, R. Hodjati, M. Azimi, *Am. J. Civ. Eng. Archit.* **2014**, *2*, 53.
- [47] Z. Zheng, B. Sun, L. Mao, *Materials* **2024**, *17*, 1189.
- [48] D. Kumar, S. Jhavar, A. Arya, K. G. Prashanth, S. Suwas, *Int. J. Fract.* **2022**, *235*, 61.
- [49] J. Bedmar, A. Riquelme, P. Rodrigo, B. Torress, J. Rams, *Materials* **2021**, *14*, 6504.
- [50] W. Ou, T. Mukherjee, G. L. Knapp, Y. Wei, T. DebRoy, *Int. J. Heat Mass Transfer* **2018**, *127*, 1084.
- [51] F.-Y. Lu, H.-Y. Wan, X. Ren, L.-M. Huang, H.-L. Liu, X. Yi, J. Iron Steel Res. Int. **2022**, *29*, 1322.
- [52] S. Hibino, T. Todo, T. Ishimoto, O. Gokcekaya, Y. Koizumi, K. Igashira, T. Nakano, *Crystals* **2021**, *11*, 1.
- [53] H. Amano, T. Ishimoto, K. Hagihara, R. Sukanuma, K. Aiba, S.-H. Sun, P. Wang, T. Nakano, *Virtual Phys. Prototyping* **2023**, *18*, e2169172.
- [54] C. Chua, Y. Liu, R. J. Williams, C. Kai Chua, S. Leong Sing, *J. Manuf. Syst.* **2024**, *73*, 79.
- [55] D. Palmeri, G. Buffa, G. Pollara, L. Fratini, *Mater. Sci. Eng. A* **2022**, *830*, 142306.
- [56] G. Kaya, U. Köklü, T. O. Ergüder, F. Cengiz, F. Yildiz, *Mater. Test.* **2023**, *65*, 1571.
- [57] T. Ronneberg, C. M. Davies, P. A. Hooper, *Mater. Des.* **2020**, *189*, 108481.
- [58] H. Carassus, J. D. Guérin, H. Morvan, G. Hauou, T. Sadat, S. Guérand, *Mater. Sci. Eng. A* **2022**, *835*, 142683.
- [59] N. Yang, J. Yee, B. Zheng, K. Gaiser, T. Reynolds, L. Clemon, W. Y. Lu, J. M. Schoenung, E. J. Lavernia, *J. Therm. Spray Technol.* **2017**, *26*, 610.

- [60] G. Huang, K. Wei, J. Deng, M. Liu, X. Zeng, *J. Manuf. Process.* **2022**, 83, 235.
- [61] K. Prasad, M. Obana, A. Ito, S. Torizuka, *Mater. Charact.* **2021**, 179, 111379.
- [62] J. K. Han, X. Liu, I. Lee, Y. O. Kuzminova, S. A. Evlashin, K.-D. Liss, M. Kawasaki, *Mater. Lett.* **2021**, 302, 130364.
- [63] G. Gottstein, *Physical Foundations of Materials Science*, Springer, Berlin Heidelberg **2013**.
- [64] M. Shamsujjoha, S. R. Agnew, J. M. Fitz-Gerald, W. R. Moore, T. A. Newman, *Metall. Mater. Trans. A* **2018**, 49, 3011.
- [65] S. Chen, G. Ma, G. Wu, A. Godfrey, T. Huang, X. Huang, *Mater. Sci. Eng. A* **2022**, 832, 142434.
- [66] L. Liu, Q. Ding, Y. Zhong, J. Zou, Y.-L. Chiu, J. Li, Q. Yu, Z. Shen, *Mater. Today* **2018**, 21, 354.
- [67] Y. Hong, C. Zhou, Y. Zheng, L. Zhang, J. Zheng, *Mater. Sci. Eng. A* **2021**, 799, 140279.
- [68] I. Gutierrez-Urrutia, D. Raabe, *Acta Mater.* **2011**, 59, 6449.
- [69] J. Su, D. Raabe, Z. Li, *Acta Mater.* **2019**, 163, 40.
- [70] S. W. Wu, G. Wang, J. Yi, Y. D. Jia, I. Hussain, Q. J. Zhai, P. K. Liaw, *Mater. Res. Lett.* **2017**, 5, 276.
- [71] X. Feaugas, *Acta Mater.* **1999**, 47, 3617.
- [72] A. Saeed-Akbari, L. Mosecker, A. Schwedt, W. Bleck, *Metall. Mater. Trans. A* **2012**, 43, 1688.